Largest eigenvalue statistics of wavefront shaping in complex media

Grégory Schehr^{1,*} and Hasan Yılmaz^{2,†}

¹Sorbonne Université, Laboratoire de Physique Théorique et Hautes Energies CNRS UMR 7589, 4 Place Jussieu, 75252 Paris Cedex 05, France ²Institute of Materials Science and Nanotechnology, National Nanotechnology Research Center (UNAM), Bilkent University, 06800 Ankara, Turkey

In wavefront shaping, waves are focused through complex media onto one or more target points, and the resulting intensity enhancement is quantified by the enhancement factor. While reproducible enhancement is crucial in experiments, the fluctuations of the enhancement factor remain largely unexplored. Here, we combine experiments, simulations, and exact analytical results using random matrix theory to determine its full distribution in multi-point focusing. Our theoretical framework goes beyond the Marčenko-Pastur law—valid only in the limit of a large number of channels—by accurately predicting the mean enhancement in finite-channel experiments and its fluctuations whenever long-range mesoscopic correlations are negligible (e.g., in weakly scattering media or under limited wavefront control). Notably, in the strongly scattering regime, experiments and simulations reveal giant fluctuations in the enhancement factor, which we attribute directly to long-range mesoscopic correlations. From a fundamental perspective, our results provide a direct method for quantifying long-range correlations in wavefront-shaping-based focusing, even with a limited number of input control channels. On the applied side, they enable the accurate prediction of the enhancement factor and a lower bound on its fluctuations, which are crucial for biomedical imaging, optical metrology, optical trapping, and communication through scattering media.

INTRODUCTION

Wavefront shaping stands as a paradigm-shifting framework for the coherent control of waves in disordered media, opening unprecedented avenues for the manipulation of complex wave phenomena [1–8]. Experimental demonstrations have shown that by precisely tailoring the incident wavefront, the total transmission of microwaves, acoustic, elastic, or optical waves can be dramatically enhanced—or waves can even be tightly focused—through strongly scattering media [1, 9-19]. This level of precise coherent control over optical waves holds profound implications for imaging [11, 20–23], quantum secure optical authentication [24], high-dimensional quantum optics [25–27], optical manipulation [28], photothermal therapy [3, 29], microsurgery [30], and optogenetics in complex scattering environments [31–33], including biological tissue, ensembles of micro-nanoparticles, and other seemingly opaque media.

The measurement of the transmission trix—encoding the input-output field relationship of a medium—is essential for controlling the output field via input wavefront shaping [34]. Once known, the transmission matrix enables focusing light to single or multiple target positions [1, 11, 17, 20–28, 31–42], or transmitting images through scattering media [43]. In particular, simultaneous focusing on multiple positions has important applications in optical metrology [37], optical trapping of microparticles [28], programmable multiport optical circuits [25–27], and focusing on extended guide stars [32, 33, 36, 44]. A key metric for evaluating the efficacy of wavefront shaping in these contexts is

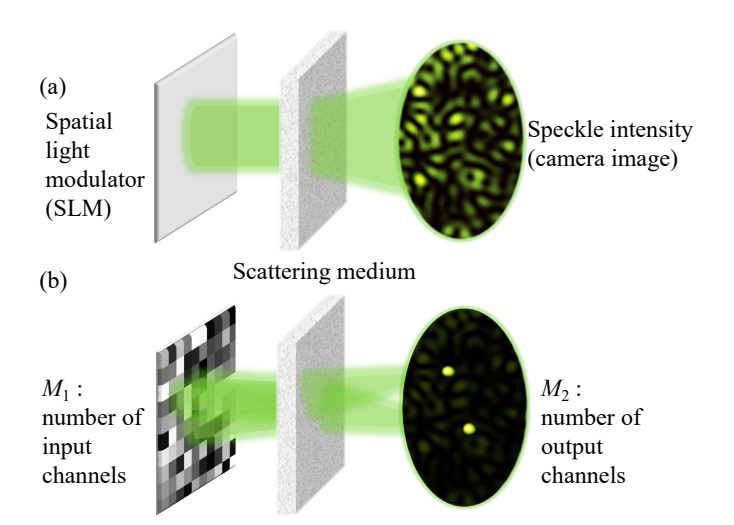


FIG. 1. The wavefront-shaping concept to focus light through a scattering medium onto multiple target points is shown. (a) A sketch of the speckle pattern in transmission when an unshaped wavefront is incident onto a scattering medium is demonstrated. (b) The incident wavefront is shaped by a spatial light modulator with M_1 degrees of freedom at the input, focusing light onto two selected target points (output channels) $M_2 = 2$.

the enhancement factor, which quantifies the intensity enhancement achieved at the target positions [1, 4, 36]. It is defined as $\eta = \sum_m |t_{mn}E_n^{\rm opt}|^2/\sum_m |t_{mn}E_n|^2$, where t_{mn} is the $M_2 \times M_1$ sub-transmission matrix of the medium, with n labelling the incident Fourier components at the input and m the position of the targets at the output. Here M_1 denotes the number of degrees of freedom at the input while M_2 denotes

the number of target (focusing) points, see Fig. 1. The vector E_n^{opt} is the input wavefront that maximizes the total intensity over these M_2 targets. The denominator in the definition of η is the same total intensity, but averaged over statistically equivalent disorder realizations (i.e. over different transmission matrices t_{mn}) or, equivalently, over independent unit-power input wavefronts E_n whose complex field components are independent and identically distributed (i.i.d.) circularly symmetric complex Gaussian entries.

One typically employs an optimization algorithm to determine the optimal input wavefront E_n^{opt} that maximizes the intensity at the target locations [4, 45]. For a single target $(M_2 = 1)$, digital optical phase conjugation attains the global maximum of the enhancement factor η [4]. For multiple targets $(M_2 > 1)$, the global maximum of η equals the largest eigenvalue $\lambda_{\rm max}$ of the focusing operator $A^{\dagger}A$, where A denotes a normalized $M_2 \times M_1$ sub-transmission matrix of the disordered medium with $Var(A) = 1/M_2$ (see e.g. [17]). In practical wavefront-shaping focusing experiments, one typically operates in the regime $M_1 \gg M_2$. The dependence of the mean enhancement $\langle \lambda_{\text{max}} \rangle$ on the number of controlled degrees of freedom M_1 and output targets M_2 has been observed experimentally and is widely recognized in the wavefront shaping community, to exhibit the scaling $\langle \lambda_{\text{max}} \rangle \sim M_1/M_2$ [4, 32, 36, 44]. On the other hand, if one assumes that the entries of A are independent complex Gaussian numbers, then the focusing operator is an (anti)-Laguerre-Wishart (LW) random matrix [46]. In this case, for large M_1 , and M_2 with the ratio M_1/M_2 fixed, $\langle \lambda_{\text{max}} \rangle$ is given by the celebrated Marčenko-Pastur (MP) law namely [47–49]

$$\langle \lambda_{\text{max}} \rangle = \left(\sqrt{\frac{M_1}{M_2}} + 1 \right)^2.$$
 (1)

While the MP law predicts $\langle \lambda_{\text{max}} \rangle \sim M_1/M_2$ in the limit $M_1 \gg M_2$, the applicability of this formula (1) in experimental situations where M_1 and M_2 are finite remains questionable.

Furthermore, predicting the sample-to-sample and target-to-target fluctuations of the enhancement factor, i.e., $\Delta \lambda_{\text{max}} \equiv \sqrt{\langle \lambda_{\text{max}}^2 \rangle - \langle \lambda_{\text{max}} \rangle^2}$, is key to establishing the fundamental limits of experimental reproducibility. Yet, its full statistical distribution and fluctuations remain largely unexplored, apart from the simpler case of single-point focusing $(M_2 = 1)$, which can be analysed rather straightforwardly [50].

In this work, we introduce a random matrix formalism that captures the full distribution of the enhancement factor for focusing light onto multiple target locations $(M_2 > 1)$ through diffusive media. Our theory accurately predicts the mean enhancement factor in finite M_1 and M_2 regimes, beyond the validity of the MP law, while also capturing its fluctuations around the

mean. This framework establishes scaling laws for the enhancement factor and its fluctuations in the absence of long-range correlations. It is known that while long-range mesoscopic correlations do not affect the mean enhancement factor, they increase the background intensity, which becomes experimentally observable for large values of M_1 [10, 17, 51, 52]. An outstanding question is whether long-range mesoscopic correlations [53–59] influence the second-order statistics of the enhancement factor. Our experiments and simulations provide a definitive answer to this question: they induce giant fluctuations that exceed the predictions of the LW random-matrix model, revealing correlation-driven deviations from the LW baseline.

From a fundamental perspective, our theory provides a direct route to quantify long-range correlations in wavefront-shaping-based focusing, even with a few input channels M_1 and a single output channel $M_2 = 1$. From an applied perspective, it enables accurate prediction of the enhancement factor and the lower bound of its fluctuations, which is crucial for applications in biomedical imaging, optical metrology, optical trapping, and optical communication through scattering media.

TRANSMISSION-MATRIX MEASUREMENTS AND ENHANCEMENT STATISTICS

The transmission matrix of a scattering medium provides the information required to modulate the incident wavefront with a spatial light modulator (SLM) and focus light onto single or multiple target points, as illustrated in Fig. 1: an unmodulated beam produces a random speckle pattern [Fig. 1(a)], whereas a shaped input beam enables simultaneous focusing at multiple target points [Fig. 1(b)].

Experimentally, we measure the transmission matrix t of a scattering sample using phase-shifting interferometry [60], see Supplementary Materials Section III for details and a sketch of the experimental setup. The scattering sample consists of a densely packed zinc oxide (ZnO) nanoparticle layer on a cover slip, with a thickness of approximately 10 µm, much larger than the transport mean free path $l_t=1$ µm, ensuring that light transport within the ZnO layer is diffusive. In our measured t_{mn} , the input channel n corresponds to a 9 × 9 SLM segment (\approx one Fourier component on the front surface). The output channel m corresponds to a position on the back surface, i.e., t_{mn} maps the SLM field to the outgoing field at the back surface.

Starting from the experimental transmission matrix t_{mn} , we generate an ensemble of focusing operators $A^{\dagger}A$, with A denoting a randomly chosen sub-transmission matrix of size $M_2 \times M_1$. We work in the regime $M_1 \gg M_2$, with $M_1 \in [100, 1000] \cap \mathbb{Z}$ and $M_2 \in [1, 5] \cap \mathbb{Z}$. Each sub-matrix A is formed by randomly selecting M_1 in-

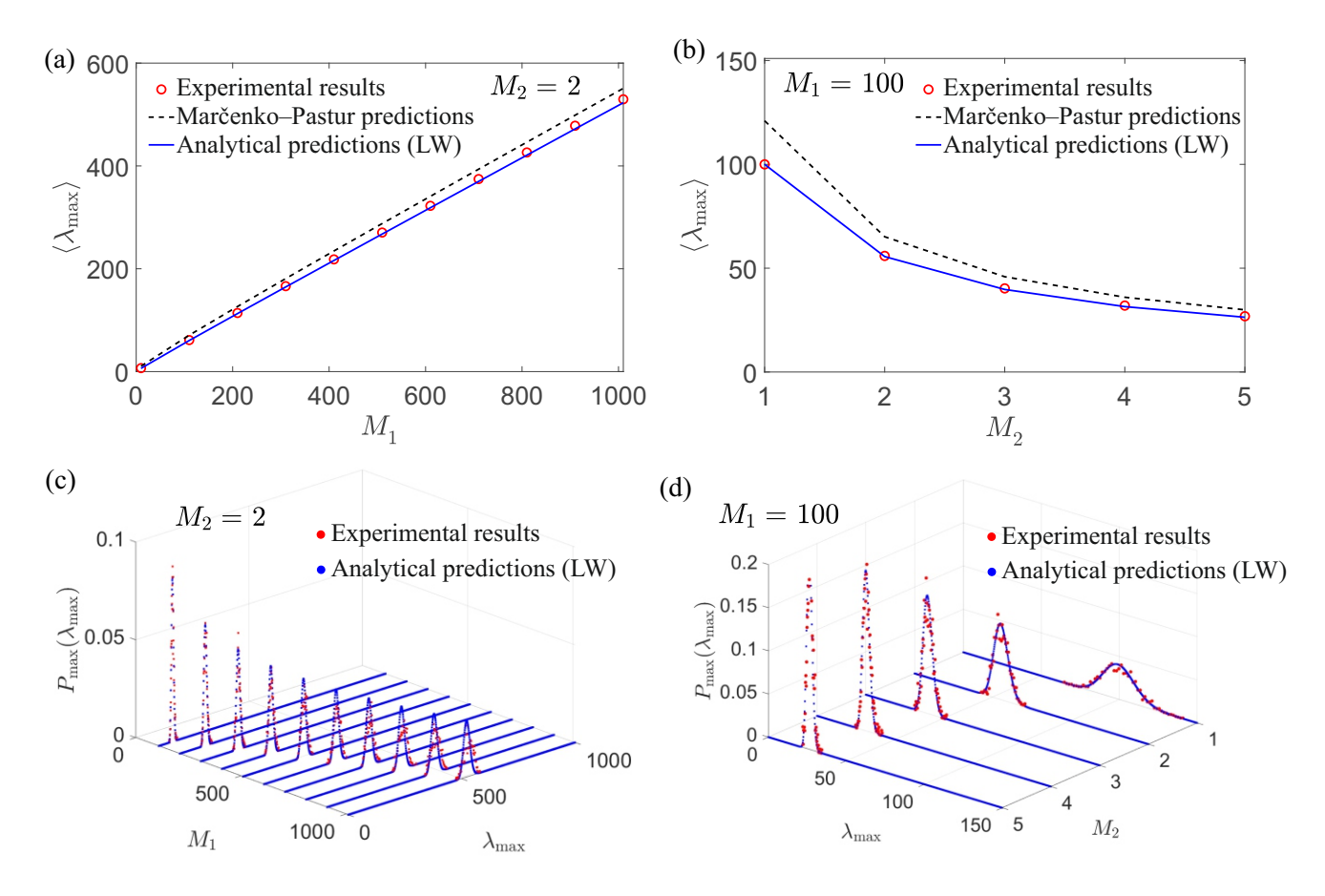


FIG. 2. The mean and probability density of the enhancement factor λ_{max} are shown. The mean enhancement $\langle \lambda_{\text{max}} \rangle$ is plotted versus the number of input channels M_1 at fixed $M_2 = 2$ (a) and versus the number of output channels M_2 at fixed $M_1 = 100$ (b). The predictions from our LW ensemble theory (solid blue) obtained from the exact analytical result in (4) agree quantitatively with the experiments (red open circles), whereas clear deviations from the Marčenko-Pastur law (dashed black) are clearly visible in panels (a,b). With no fitting parameter, the predicted probability densities $P(\lambda_{\text{max}}) = Q'_{\text{max}}(\lambda_{\text{max}})$ from Eq. (4) likewise match quite well the experimental distributions for small M_1 in (c) and for all values of M_2 for $M_1 = 100$ in (d).

put segments on the SLM and M_2 output target focusing positions m in transmission. For each sub-matrix size $M_2 \times M_1$, we compute its eigenvalues via $A^\dagger A V_\alpha = \lambda_\alpha V_\alpha$. We then determine the probability density $P_{\rm max}(\lambda_{\rm max})$, the mean $\langle \lambda_{\rm max} \rangle$, and the standard deviation $\Delta \lambda_{\rm max}$ of the largest eigenvalue of the associated focusing operator, thereby obtaining the experimental statistical distribution of the enhancement factor for light focusing through the scattering sample.

In Fig. 2, we present the experimental and theoretical largest eigenvalues λ_{max} (i.e., enhancement values η) and their probability densities $P_{\text{max}}(\lambda_{\text{max}})$ for various numbers of input (M_1) and output (M_2) channels. The scaling of λ_{max} with M_1 [Fig. 2(a)] and with M_2 [Fig. 2(b)] predicted by our LW random-matrix-based analytical theory is in excellent agreement with the experimental values, whereas the Marčenko-Pastur prediction (1) shows a clear deviation. This deviation

arises because the Marčenko-Pastur law is exact only in the asymptotic limit of large M_1 and M_2 , while our LW random-matrix-based theory remains accurate for finite M_1 and M_2 . Moreover, our theory predicts not only the mean of λ_{\max} but also its full distribution $P_{\max}(\lambda_{\max})$, as shown in Figs. 2(c,d). The theoretical prediction of $P_{\max}(\lambda_{\max})$ agrees well with the experimental $P_{\max}(\lambda_{\max})$ at small M_1 . However, as M_1 increases, the experimental distribution broadens relative to the theoretical one (Fig. 2(c)). For $M_1 = 100$, the experimental and theoretical probability densities are in close agreement for all investigated values of $M_2 \in [1,5] \cap \mathbb{Z}$ (Fig. 2(d)).

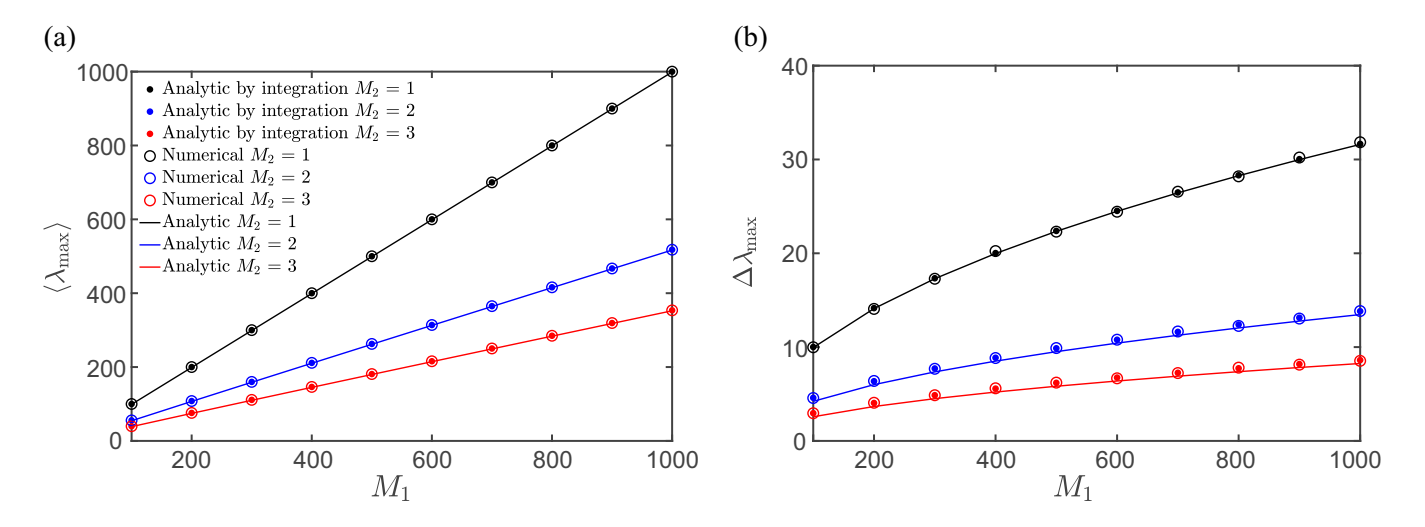


FIG. 3. Panels (a) and (b) show respectively the mean and the standard deviation of the largest eigenvalue, λ_{max} (i.e., the enhancement factor), as a function of the number of input channels M_1 , for different numbers of target channels $M_2 = 1, 2, 3$ (indicated by color). Open circles denote numerical results obtained from Laguerre-Wishart (LW) matrices, while solid circles correspond to the exact analytical predictions derived from the cumulative distribution function of λ_{max} [Eq. (4)]. Solid lines show the asymptotic large- M_1 results [Eqs. (19) and (6)], demonstrating excellent agreement between numerical, exact, and asymptotic results.

RANDOM-MATRIX FRAMEWORK: THE LAGUERRE-WISHART ENSEMBLE

Having presented the main theoretical findings and discussed them in the context of our experimental results, we now detail the random-matrix framework from which they are derived. Our theoretical approach is based on an analytic treatment of the spectral properties of the focusing operator in a random matrix setting. For this, we consider the case where the entries of the $M_2 \times M_1$ subtransmission matrix A are independent complex Gaussian variables. The corresponding focusing operator $A^{\dagger}A$ is thus an $M_1 \times M_1$ random matrix. Since $M_1 > M_2$, it belongs to the complex anti-LW ensemble [46] where "anti" indicates that the matrix is rectangular with more columns than rows [61–63]. In this case, $A^{\dagger}A$ has exactly M_2 positive eigenvalues $\lambda_1, \ldots, \lambda_{M_2}$, while the remaining $M_1 - M_2$ eigenvalues vanish.

These nonzero eigenvalues encode the strength of the transmission channels. Since the matrix A is random, so are these nonzero eigenvalues, which thus fluctuate from one sample of A to another. However, it turns out that their joint (i.e., multivariate) statistics are known exactly. Indeed, their joint probability density function (JPDF) reads [61, 62]

$$P(\lambda_1, \dots, \lambda_{M_2}) = \frac{1}{Z} \prod_{i=1}^{M_2} \lambda_i^{\nu} e^{-M_2 \lambda_i} \prod_{i < j} (\lambda_i - \lambda_j)^2, \quad (2)$$

where $\nu = M_1 - M_2 > 0$ and Z is a normalization factor that can be computed explicitly. From this JPDF (2), the average density of eigenvalues, defined as $\rho(\lambda) =$ $\sum_{i=1}^{M_1} \langle \delta(\lambda - \lambda_i) \rangle$ where δ is a Dirac delta-function and $\langle \cdots \rangle$ denotes an average over the JPDF in (2), can be computed explicitly. It is simply obtained by integrating the JPDF (2) over $\lambda_2, \cdots, \lambda_{M_1}$ while keeping $\lambda_1 \equiv \lambda$ fixed. This multiple integral can be carried out explicitly and it reads $\rho(\lambda) = \nu \delta(\lambda) + \tilde{\rho}(\lambda)$ where the density of nonzero eigenvalues is given by (see e.g. [64])

$$\tilde{\rho}(\lambda) = M_2^{\nu+1} \lambda^{\nu} e^{-M_2 \lambda} \sum_{k=0}^{M_2 - 1} \frac{k!}{(k+\nu)!} [L_k^{(\nu)}(M_2 \lambda)]^2 , \quad (3)$$

where $L_k^{(\nu)}(\lambda)$ is the generalized Laguerre polynomial of index ν and degree k.

Of particular interest is the statistics of the largest eigenvalue $\lambda_{\max} = \max\{\lambda_1, \dots, \lambda_{M_1}\}$, which in the context of wavefront shaping corresponds directly to the enhancement factor [17]. Rather than computing its probability density function $P_{\max}(x) = \operatorname{Prob}(\lambda_{\max} = x)$, it is often more convenient to consider the cumulative distribution function $Q_{\max}(x) = \operatorname{Prob}(\lambda_{\max} \leq x) = \int_0^x P_{\max}(x') dx'$ [65]. Indeed, the event $\lambda_{\max} \leq x$ is equivalent to all eigenvalues satisfying $\lambda_i \leq x$ for $i = 1, \dots, M_1$. Therefore, $Q_{\max}(x)$ can be obtained by integrating the joint probability density function in (2) over the hypercube $[0, x]^{M_1}$. This multiple integral can be evaluated explicitly using standard techniques from random matrix theory and determinantal processes, yielding (see also [66, 67])

$$Q_{\max}(x) = A_{M_1, M_2} \det_{1 \le i, j \le M_2} \left[\gamma(i+j-1+\nu, M_2 x) \right], (4)$$

where $\gamma(s,z)=\int_0^z t^{s-1}e^{-t}\,dt$ is the lower incomplete gamma function (which in our case can be simply ex-

pressed in terms of exponentials and polynomials) and $A_{M_1,M_2} = M_2!/(\prod_{k=0}^{M_2-1}(k+1)!(k+\nu)!)$ is a normalization constant (independent of x). As $x \to 0$ it behaves as $Q_{\max}(x) \sim x^{M_1M_2}$ while $1 - Q_{\max}(x) \sim q_{M_1}(x)e^{-M_2x}$ as $x \to \infty$ where $q_{M_1}(x)$ is a polynomial of order $M_1 + 1$.

This $M_2 \times M_2$ determinant in Eq. (4) is straightforward to evaluate numerically (for moderate values of M_2), allowing a direct computation of the mean $\langle \lambda_{\text{max}} \rangle$ and fluctuations $\Delta \lambda_{\text{max}}$. This exact characterization (4) is particularly useful in wavefront shaping experiments, where M_2 is typically small. As discussed earlier in the previous section, Fig. 2 revisits the behavior of the largest eigenvalue, but now emphasizes the exact finite-size analytical predictions. In Fig. 2(a,b), we use Eq. (4) to compute the theoretical curves for $\langle \lambda_{\rm max} \rangle$ and confront them with the experimental values, finding excellent agreement for all investigated M_1 and M_2 . At the same time, these panels clearly reveal a deviation from the MP prediction (1), which is expected since the MP law strictly applies in the limit where both M_1 and M_2 are large, whereas here $2 \leq M_2 \leq 5$. In Fig. 2(c,d), we further use $P_{\text{max}}(x) = dQ_{\text{max}}(x)/dx$ with $Q_{\text{max}}(x)$ given in Eq. (4) to generate the analytical curves for the full distribution of $\lambda_{\rm max}$ and compare them against the experimentally obtained histograms, which remains in excellent agreement for small M_1 .

As we mentioned earlier, in wavefront shaping experiments, one is often interested in the limit where $M_1 \gg M_2$. In this limit, one can show that the complex LW ensemble in (2) converges, up to a rescaling of the eigenvalues by M_1 to the so-called Gaussian Unitary Ensemble (GUE) that describes Hermitian matrices with independent (complex) Gaussian entries. Consequently for large $M_1 \gg M_2$ one finds

$$\langle \lambda_{\text{max}} \rangle \approx \frac{1}{M_2} \left(M_1 + \sqrt{2 M_1} \langle \mu_{\text{max}} \rangle \right) ,$$
 (5)

where $\langle \mu_{\rm max} \rangle$, which only depends on M_2 and not on M_1 , denotes the average value of the largest eigenvalue of a GUE matrix of size $M_2 \times M_2$. For example, one finds $\langle \mu_{\rm max} \rangle = \{0, \sqrt{2/\pi}, 27/(8\sqrt{2\pi})\}$ for $M_2 = \{1, 2, 3\}$ respectively (for further details, see Sec. I.C. of the Supplemental Material). In the limit $M_2 \gg 1$ one has $\langle \mu_{\rm max} \rangle \approx \sqrt{2M_2}$ and this formula (19) coincides at leading order with the Marčenko-Pastur prediction given in Eq. (1) in the main text, in the limit $M_1/M_2 \gg 1$. However, for finite M_2 , the average value $\langle \mu_{\rm max} \rangle$ differs from $\sqrt{2M_2}$ and therefore the large M_1 estimate in (19) differs from the Marčenko-Pastur prediction. This formula (19) ultimately enables a more accurate description of experimental data.

Similarly, by exploiting the convergence of the complex LW ensemble to the GUE in the limit $M_1 \gg M_2$, one can obtain the behavior of the standard deviation $\Delta \lambda_{\text{max}}$ in

this limit. One finds indeed

$$\Delta \lambda_{\text{max}} \approx \frac{\sqrt{2M_1}}{M_2} \Delta \mu_{\text{max}} ,$$
 (6)

where $\Delta\mu_{\rm max}$, which depends only on M_2 , is the standard deviation of the largest eigenvalue of a GUE matrix of size $M_2 \times M_2$. It can be computed explicitly for the first few values of M_2 (for further details, see Sec. I.C. of the Supplemental Material). These asymptotic behaviors for the mean (19) and the standard deviation (6) are compared to numerical and exact calculations in Fig. 3, showing a good agreement.

We conclude this section by noting that in the opposite limit, when both M_1 and M_2 are large with a fixed ratio, the eigenvalue density converges to the Marčenko-Pastur law, supported on $[x_-, x_+]$ with $x_{\pm} = (\sqrt{M_1/M_2 \pm 1})^2$. In this limit, λ_{max} concentrates near x_+ , with fluctuations of order $M_2^{-2/3}$ governed by the celebrated Tracy– Widom (TW) distribution [68–70] (for a review see [71]), recovering the approximation used in Eq. (1). This formula (4) thus provides both the exact finite- M_2 statistics of λ_{max} and the asymptotic large- M_1 , M_2 behavior, bridging theoretical insight and experimental relevance. Extreme eigenvalue statistics in the TW regime have been observed experimentally in other physically distinct systems in the large-size limit, such as interface growth in nematic liquid crystals [72], coupled lasers [73], and dissipative many-particle systems [74]. In contrast, our experiments probe the largest eigenvalue of finite-size LW matrices in a wavefront-shaping setting, where the distribution generically deviates from TW statistics.

THE ROLE OF LONG-RANGE MESOSCOPIC CORRELATIONS IN ENHANCEMENT-FACTOR FLUCTUATIONS

Our analytical theory provides the full probability distribution of the largest eigenvalue and thus predicts its fluctuations through the standard deviation $\Delta \lambda_{\rm max}$. In Figs. 4(a,b), we plot the experimentally measured $\Delta \lambda_{\rm max}$ as functions of M_1 and M_2 , together with the correlation-free LW-based predictions. For small input-channel numbers, $M_1 \lesssim 100$, the theory reproduces the experimental fluctuations. For larger M_1 , however, the theory increasingly underestimates the fluctuations, consistent with the broader experimental $P_{\rm max}(\lambda_{\rm max})$ compared to the LW prediction (Fig. 2(c)).

The LW-based framework is built on correlation-free random matrices. In contrast, it is well established that the transmission matrix of a disordered medium exhibits long-range mesoscopic correlations [53–59]. The systematic excess of the experimental fluctuations over the LW prediction in Figs. 4(a,b) therefore naturally raises the question of whether the observed fluctuations of the largest eigenvalue (i.e., the enhancement factor)

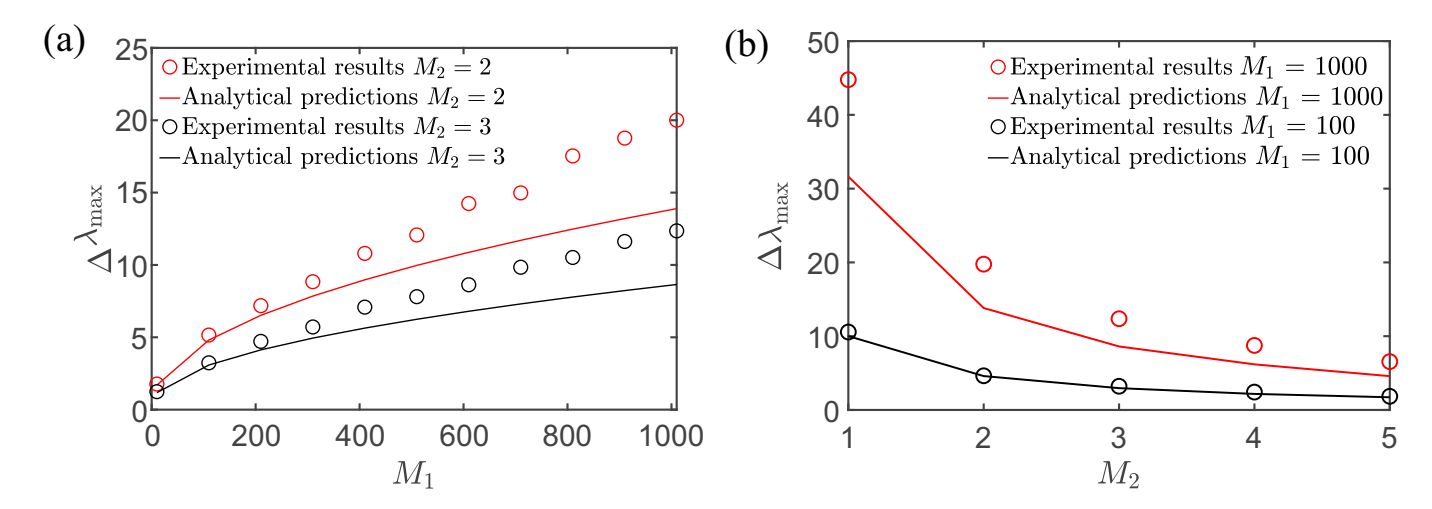


FIG. 4. Fluctuations of the enhancement factor, quantified by the standard deviation $\Delta \lambda_{\text{max}} \equiv \sqrt{\langle \lambda_{\text{max}}^2 \rangle} - \langle \lambda_{\text{max}} \rangle^2$, are shown versus the number of input channels M_1 at fixed $M_2 = 2$ and $M_2 = 3$ (a) and versus the number of output channels M_2 at fixed $M_1 = 100$ and $M_1 = 1000$ (b). Our LW-ensemble theory (solid lines) agrees well with the experiments (open circles) up to $M_1 \approx 100$ in (a) and for all M_2 at fixed $M_1 = 100$ in (b). For $M_1 > 100$, the experiments exhibit larger fluctuations than predicted (a,b), which are attributable to long-range mesoscopic correlations within the sample.

in wavefront-shaping focusing experiments originate from such long-range correlations.

To address this question and systematically assess the role of long-range correlations—which are known to increase with sample thickness [17, 53, 75]—we performed numerical simulations for slabs of varying thicknesses. Specifically, we computed the field transmission matrix t of two-dimensional (2D) scattering slabs with normalized thicknesses $k_0L = 1, 50, 200$ and normalized transport mean free path $k_0l_t = 20.6$ using a recursive Green's function algorithm [76, 77], where $k_0 = 2\pi/\lambda_0$ denotes the wavenumber corresponding to the wavelength λ_0 .

For each slab thickness, we systematically obtained the mean largest eigenvalue $\langle \lambda_{\rm max} \rangle$ —averaged over different focusing target positions—and its standard deviation $\Delta \lambda_{\rm max}$ for sub-transmission matrices of various sizes $M_2 \times M_1$ (see Supplemental Material, Sec. II).

In Fig. 5, we show the numerical, analytical, and experimental results for both the mean and the standard deviation of the largest eigenvalue. As seen in Figs. 5(a,b), the numerical mean largest eigenvalue $\langle \lambda_{\rm max} \rangle$ (i.e., the enhancement factor η) scales with the number of input channels M_1 and the number of output channels M_2 in excellent agreement with our LW-random-matrix-based analytical theory and with the experiments, for all slab thicknesses. This behavior is expected because long-range correlations do not affect the enhancement factor [10, 17]: consequently, increasing the slab thickness does not change the mean enhancement.

The situation is different for the fluctuations. In Figs. 5(c,d), we observe a clear increase in the standard deviation $\Delta \lambda_{\rm max}$ of the largest eigenvalues as the slab becomes thicker in the simulations, which is a clear sig-

nature of long-range mesoscopic correlations governing these fluctuations. Moreover, our simulation results show that the observed fluctuations can be several times larger than the correlation-free LW prediction, thus indicating that long-range mesoscopic correlations can give rise to giant fluctuations of the enhancement factor, far beyond the finite-size random-matrix baseline.

Remarkably, even for extremely thin slabs $(L \ll$ l_t), the fluctuations already start to deviate from the correlation-free prediction as M_1 increases (Fig. 5(c)), and the experimental data show the same trend. One might expect even larger deviations in the experiment, since the sample is much thicker than a transport mean free path $(L \gg l_t)$. However, the observable strength of long-range correlations decreases with the input-control ratio M_1/g , where g is the dimensionless conductance or number of open channels [15, 17, 78]. Because our experimental slab is three-dimensional (3D), q is much larger than in the 2D simulations, and therefore the effective input-control ratio is substantially smaller. This reduced control weakens the impact of long-range correlations on $\Delta \lambda_{\rm max}$ in the experiment, explaining the quantitative differences while preserving the qualitative agreement.

Traditionally, long-range correlations are revealed through the variance of the eigenvalue density of $t^{\dagger}t$ or through shifts in $\langle \lambda_{\rm max} \rangle$, but this requires measuring large transmission matrices with $M_1 \gtrsim 2000$ inputs and $M_2 \gtrsim 3000$ outputs through very thick samples ($\approx 50 l_t$) [17]. In contrast, we show here that long-range correlations can be detected from much smaller datasets—using submatrices with only $M_1 \lesssim 200$ and even a single output channel ($M_2 = 1$)—and through samples as thin as $\approx 10 l_t$. This is possible because the

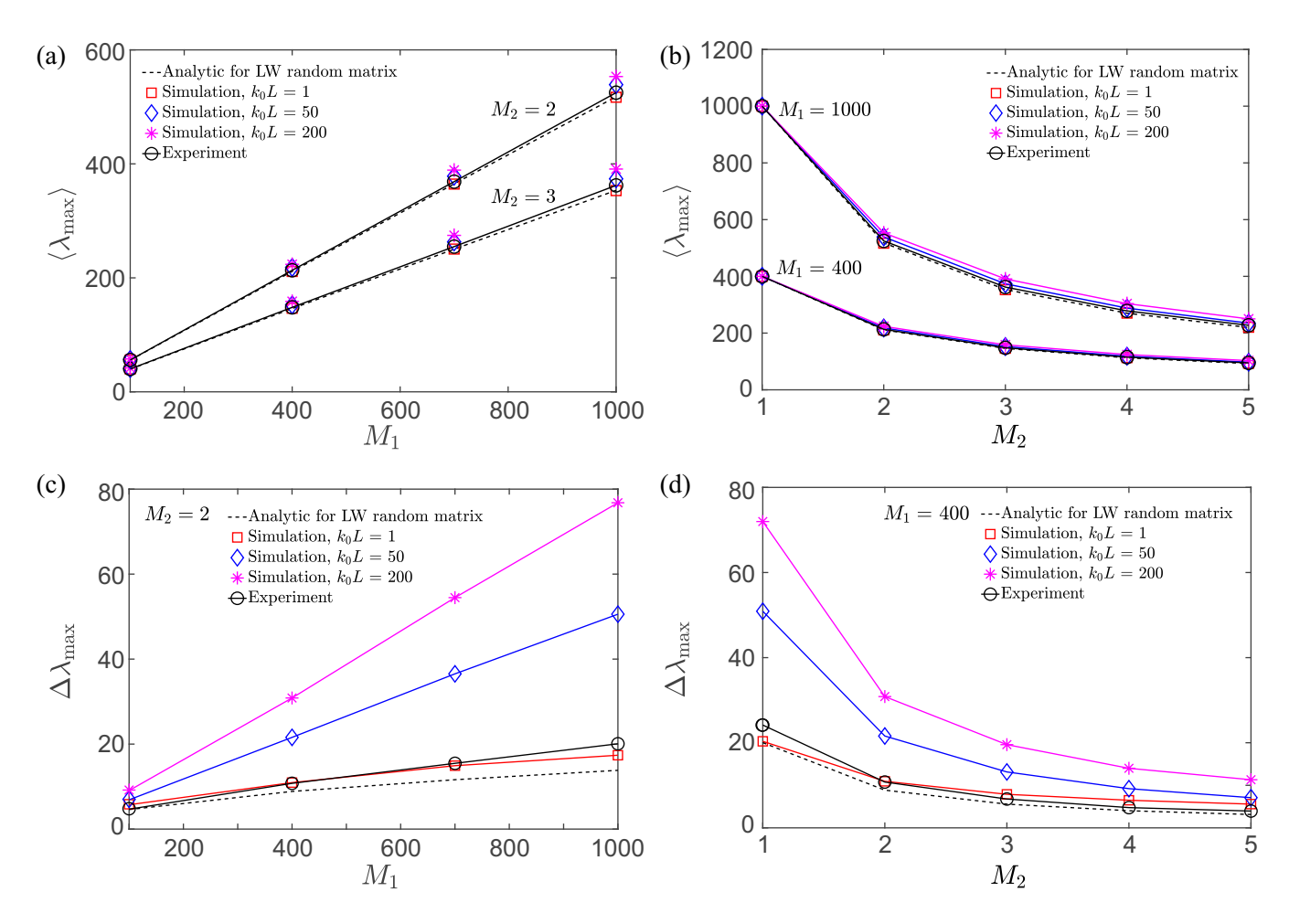


FIG. 5. The mean enhancement $\langle \lambda_{\text{max}} \rangle$ versus the number of input channels M_1 at fixed $M_2=2$ and $M_2=3$ (a) and versus the number of output channels M_2 at fixed $M_1=400$ and $M_1=1000$ are shown for our analytic LW-ensemble theory (dashed black line), experiments (black open circles), and numerical simulations (red open squares for $k_0L=1$, blue open diamonds for $k_0L=50$, and magenta asterisks for $k_0L=200$, all with normalized transport mean free path $k_0l_t=20.6$). All results agree across M_1 and M_2 , demonstrating that long-range mesoscopic correlations do not affect the mean enhancement. Fluctuations, quantified by the standard deviation $\Delta \lambda_{\text{max}} \equiv \sqrt{\langle \lambda_{\text{max}}^2 \rangle} - \langle \lambda_{\text{max}} \rangle^2$ versus the number of input channels M_1 at fixed $M_2=2$ (c), and versus the number of output channels M_2 at fixed $M_1=400$ (d), exhibit a slight experimental excess and a pronounced excess in simulations, which grows with slab thickness. These giant fluctuations in thick slabs reveal long-range mesoscopic correlations beyond the correlation-free LW model.

LW-based analytical framework provides exact predictions in the absence of correlations, allowing any systematic excess in fluctuations to be unambiguously attributed to long-range mesoscopic correlations.

DISCUSSION AND CONCLUSIONS

In conclusion, our work establishes the statistical foundations of the enhancement factor, a key measure of coherent control of light through complex media with implications for biomedical imaging, optical metrology, secure communication, optical trapping, and quantum photonics. By combining experiments, numerical simulations, and exact random-matrix results, we determine the full probability distribution of the enhancement fac-

tor for multi-point focusing. For finite numbers of input and output channels, and within the LW-random-matrix framework (i.e., in the absence of long-range correlations), our theory quantitatively captures both the mean and the fluctuations, going beyond the Marčenko-Pastur prediction for the mean and the Tracy-Widom law for fluctuations in the asymptotic large-number-of-channels limit. These results provide, for the first time, a comprehensive statistical description directly relevant to experimentally accessible finite-channel regimes.

Beyond the LW-matrix framework, we report *giant* fluctuations of the enhancement factor in strongly scattering samples, originating from long-range mesoscopic correlations. Measuring a near-complete transmission matrix of a scattering medium grants direct access to

such correlations [78, 79]. In practice, however, a threedimensional medium can support 10⁴–10⁶ channels, making a complete transmission-matrix acquisition unfeasible; experiments therefore probe long-range correlations using submatrices with only $\sim 10^3$ channels [13, 15, 17]. Our results show that fluctuations of the enhancement factor already provide a sensitive probe of long-range correlations when only $M_1 \lesssim 200$ input and $M_2 = 1$ output channels are controlled, thereby bridging wavefrontshaping-based focusing experiments and mesoscopic wave transport, and demonstrating that random-matrix theories for the largest eigenvalue statistics break down when such correlations are omitted. Together, these results reveal that the enhancement factor—long considered a simple performance metric—is in fact a powerful statistical observable that encodes long-range mesoscopic correlations in complex media.

Existing theories either explicitly incorporate long-range mesoscopic correlations into random-matrix models and address only the global eigenvalue distribution [78], or, as in radiant-field theory [80, 81], provide an accurate global eigenvalue distribution without explicitly encoding these correlations; in both cases, they determine only the mean enhancement, but not its fluctuations. An accurate prediction of extreme eigenvalue statistics, as well as the impact of long-range mesoscopic correlations on them, thus remains an open problem. The present work motivates future theories that explicitly incorporate such correlations to complete the statistical picture.

More broadly, though realized here in an optical setting, the mechanism relies solely on multiple scattering and finite-size statistics—properties common to many wave systems. Given the universality of these ingredients, one can expect that the fluctuation physics uncovered in this work extends equally to acoustic, elastic, microwave, and matter-wave systems.

ACKNOWLEDGEMENTS

We thank Hui Cao for supporting the original transmission-matrix measurements and for providing access to the dataset, as well as for carefully reading the manuscript, Arthur Goetschy for insightful discussions, and Ilgin Yağmur Şen for initial contributions. H. Y. thanks Soner Albayrak for helpful discussions, and acknowledges support from TÜBİTAK (Grant No. 123C552) and the Science Academy's BAGEP Award, funded by the Sevinç-Erdal İnönü Foundation. G. S. acknowledges support from ANR Grant No. ANR-23- CE30-0020-01 EDIPS.

SUPPLEMENTARY MATERIALS

This document serves as supplementary materials for "Largest eigenvalue statistics of wavefront shaping in complex media." Section I presents the analytic theory, Section II provides information about wave propagation simulations, and Section III describes the details of experiments.

I. ANALYTICAL APPROACH VIA RANDOM MATRIX THEORY

In this section, we provide some details about the analytical results provided in the main text. Our starting point is the joint probability distribution function (JPDF) of the M_2 real and nonzero eigenvalues given of the focusing operator $A^{\dagger}A$ in Eq. (2) of the main text, which we recall here

$$P(\lambda_1, \dots, \lambda_{M_2}) = \frac{1}{Z} \prod_{i=1}^{M_2} \lambda_i^{\nu} e^{-M_2 \lambda_i} \prod_{i < j} (\lambda_i - \lambda_j)^2 , \quad (7)$$

where $\nu = M_1 - M_2 > 0$. The normalization factor can be explicitly computed, leading to

$$Z = M_2^{-M_1 M_2} \prod_{k=0}^{M_2 - 1} [(k+1)!(k+\nu)!].$$
 (8)

Average density

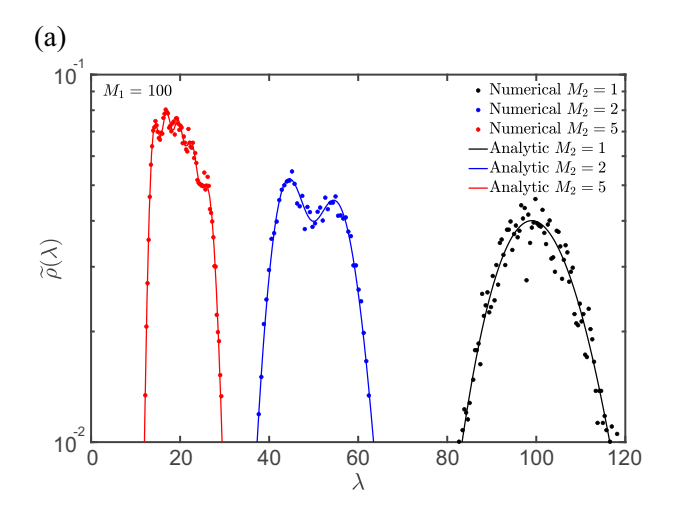
The density of nonzero eigenvalues $\tilde{\rho}(\lambda)$ is defined as

$$\tilde{\rho}(\lambda) = \sum_{i=1}^{M_2} \langle \delta(\lambda - \lambda_i) \rangle \tag{9}$$

where $\delta(x)$ denotes the Dirac delta function and with the notation $\langle \cdots \rangle$ referring to an average over the random eigenvalues $\lambda_1, \cdots, \lambda_{M_2}$ distributed according to the JPDF in (7). By inserting this explicit expression for the JPDF in Eq. (9) and using its invariance under permutation of the λ_i 's we see that computing $\tilde{\rho}(\lambda)$ amounts to perform the following multiple integral

$$\tilde{\rho}(\lambda) = M_2 \int_0^\infty d\lambda_2 \cdots \int_0^\infty d\lambda_{M_2} P(\lambda, \lambda_2, \cdots, \lambda_{M_2})$$
 (10)

It turns out that this multiple integral can be performed explicitly using standard tools in random matrix theory (RMT), e.g., orthogonal polynomials, leading to the result given in Eq. (3) of the main text. In fact, in this formula (3), the sum over k can be explicitly computed



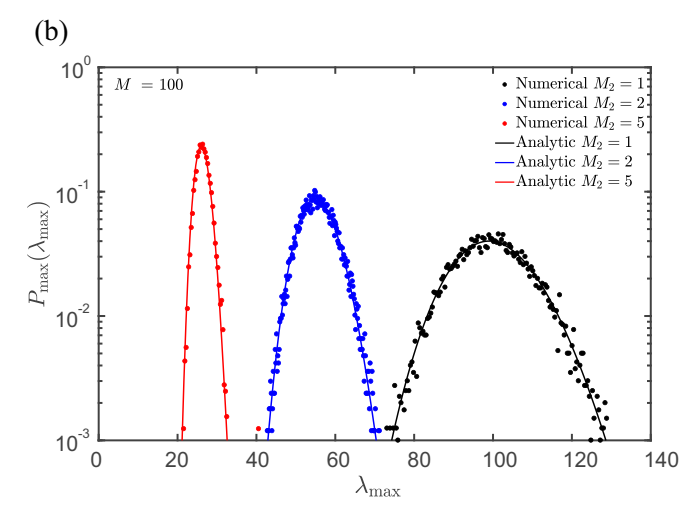


FIG. 6. (a) Eigenvalue distributions $\tilde{\rho}(\lambda)$ and (b) largest-eigenvalue distributions $P_{\text{max}}(\lambda_{\text{max}})$ for $M_1 = 100$ and $M_2 = 1, 2, 5$. The LW-random-matrix-based predictions and the numerical Wishart-matrix results coincide remarkably well for both $\tilde{\rho}(\lambda)$ given in (11) and $P_{\text{max}}(\lambda_{\text{max}}) = Q'_{\text{max}}(\lambda_{\text{max}})$ given in (18).

using the Cristoffel-Darboux relation

$$\tilde{\rho}(\lambda) = \frac{M_2! M_2^{\nu+1} \lambda^{\nu} e^{-M_2 \lambda}}{(M_2 + \nu - 1)!} \begin{bmatrix} L_{M_2 - 1}^{(\nu)}(M_2 \lambda) L_{M_2 - 1}^{(\nu+1)}(M_2 \lambda) \\ -L_{M_2}^{(\nu)}(M_2 \lambda) L_{M_2 - 2}^{(\nu+1)}(M_2 \lambda) \end{bmatrix} (11)$$

where $L_k^{(\nu)}(\lambda)$ is the generalized Laguerre polynomial of index ν and degree k. This density has a nontrivial structure exhibiting M_2 local maxima, corresponding to the typical location of the M_2 nonzero eigenvalues of the Anti-Wishart matrix $A^{\dagger}A$. Its asymptotic behaviors for small and large λ are given by

$$\tilde{\rho}(\lambda) \approx \begin{cases} C_0 \lambda^{\nu} , & \lambda \to 0 \\ C_{\infty} \lambda^{\nu + 2M_2 - 2} e^{-M_2 \lambda} , & \lambda \to \infty , \end{cases}$$
(12)

where the amplitudes C_0 and C_{∞} are given by

$$C_0 = \frac{M_2^{1+\nu}(M_2 + \nu)!}{(M_2 - 1)!\nu!(\nu + 1)!},$$
(13)

$$C_0 = \frac{M_2^{1+\nu}(M_2 + \nu)!}{(M_2 - 1)!\nu!(\nu + 1)!} , \qquad (13)$$

$$C_{\infty} = \frac{M_2^{\nu + 2M_2 - 1}}{(M_2 + \nu - 1)!(M_2 - 1)!} . \qquad (14)$$

A plot of the density given $\tilde{\rho}(\lambda)$ in Eq. (11) vs λ is shown in Fig. 6 (a) for $M_1 = 100$ and different values of $M_2 = 1, 2, 5$ along with numerical results obtained by direct diagonalization of LW matrices, demonstrating a good agreement. For $M_2 = 2$ and $M_2 = 5$, we observe two and five local maxima, respectively. These peaks reflect the typical positions of the corresponding nonzero eigenvalues of $A^{\dagger}A$. Because of eigenvalue repulsion, these eigenvalues form a relatively rigid spectrum: their individual values fluctuate, but their locations remain sharply concentrated around well-defined

mean positions. Consequently, the probability density develops distinct peaks near the characteristic positions of the first, second, third, and so on, eigenvalues. As M_2 becomes larger, these individual peaks gradually merge, and in the asymptotic limit of large M_2 (and M_1), the spectrum converges to the Marčenko-Pastur distribution.

Cumulative distribution function of λ_{max}

As explained in the main text, the cumulative distribution function (CDF) of $Q_{\text{max}}(x) = \text{Prob}(\lambda_{\text{max}} \leq x) =$ $\operatorname{Prob}(\lambda_1 \leq x, \dots, \lambda_{M_2} \leq x)$ can be written as the following multiple integral

$$Q_{\max}(x) = \int_0^x d\lambda_1 \cdots \int_0^x d\lambda_{M_2} P(\lambda_1, \dots, \lambda_{M_2}) . \quad (15)$$

This multiple integral can be performed explicitly using the standard Cauchy-Binet formula [49], leading to

$$Q_{\max}(x) = \frac{M_2!}{Z} \det \mathbb{M}, \quad \mathbb{M}_{i,j} = \int_0^x \lambda^{i+j-2+\nu} e^{-M_2\lambda} d\lambda , \qquad (16)$$

with $i, j = 1, \dots, M_2$. We recall that Z is given in Eq. (8). By expressing the integral over λ that enters the definition of the matrix elements $M_{i,j}$ in (16) in terms of the incomplete gamma function $\gamma(s,z) = \int_0^z t^{s-1}e^{-t} dt$ and performing standard manipulations of the determinant yields the expression given in Eq. (4) in the main text. In fact, since $\nu = M_1 - M_2 > 0$ is an integer, this integral over λ can be performed explicitly, leading to

$$\mathbb{M}_{i,j} = \int_0^x \lambda^{i+j-2+\nu} e^{-M_2 \lambda} d\lambda \tag{17}$$

$$= \frac{(i+j-2+\nu)!}{M_2^{i+j-1+\nu}} \left(1 - e^{-M_2 x} \sum_{k=0}^{i+j-2+\nu} \frac{(M_2 x)^k}{k!} \right),$$

which holds provided i, j and $\nu = M_1 - M_2$ are integers (which is indeed the case here). Injecting this in Eq. (16), one finds the fairly explicit expression

$$Q_{\max}(x) = \frac{M_2!}{\prod_{k=0}^{M_2-1} (k+1)! (k+\nu)!} \det_{1 \le i,j \le M_2} \left[(i+j-2+\nu)! \left(1 - e^{-M_2 x} \sum_{k=0}^{i+j-2+\nu} \frac{(M_2 x)^k}{k!} \right), \right] , \nu = M_1 - M_2 . (18)$$

Note that for $M_2=1$ one finds the simple result $P_{\max}(x)=dQ_{\max}(x)/dx=x^{M_1-1}e^{-x}/(M_1-1)!$, as in [50], but already for $M_2=2$ the expression is much more complicated.

From this explicit expression, one can obtain the asymptotic behaviors of $Q_{\max(x)}$. As $x \to 0$ it behaves as $Q_{\max}(x) \propto x^{M_1 M_2}$ while $1 - Q_{\max}(x) \to q_{M_1}(x) e^{-M_2 x}$ as $x \to \infty$, where $q_{M_1}(x)$ is a polynomial of order $M_1 + 1$.

A plot of the density given $P_{\text{max}}(\lambda_{\text{max}}) = Q'_{\text{max}}(\lambda_{\text{max}})$ from Eq. (18) vs λ_{max} is shown in Fig. 6 (b) for $M_1 = 100$ and different values of $M_2 = 1, 2, 5$ along with numerical results obtained by direct diagonalization of LW matrices, demonstrating a good agreement.

The limit of large $M_1 \gg M_2$

In the limit where $M_1\gg M_2$ one can show that the complex Wishart ensemble described by (7) converges, up to a rescaling of the eigenvalues by M_1 , to the Gaussian Unitary Ensemble (GUE) that describes Hermitian matrices with independent (complex) Gaussian entries. Consequently for large $M_1\gg M_2$ one finds

$$\langle \lambda_{\text{max}} \rangle \approx \frac{1}{M_2} \left(M_1 + \sqrt{2 M_1} \langle \mu_{\text{max}} \rangle \right) ,$$
 (19)

where μ_{max} denotes the largest eigenvalue of a GUE matrix of size $M_2 \times M_2$. Its CDF $\mathcal{Q}_{\text{max}}(x) = \text{Prob.}(\mu_{\text{max}} \leq x)$ can be computed as explained in Section , but transposed to the case of GUE. It reads

$$Q_{\max}(x) = \frac{1}{\widetilde{Z}} \det \widetilde{\mathbb{M}} , \ \widetilde{\mathbb{M}}_{i,j} = \int_{-\infty}^{x} \mu^{i+j-2} e^{-\mu^{2}} d\mu , \ (20)$$

with $\tilde{Z} = \det_{i,j=1}^N \int_{-\infty}^\infty \mu^{i+j-2} \, e^{-\mu^2} d\mu$. From this expression for the CDF in (20) one can obtain the average $\langle \mu_{\text{max}} \rangle = \int_{-\infty}^\infty x \mathcal{Q}'_{\text{max}}(x) dx$ yielding in particular

$$\langle \mu_{\text{max}} \rangle = \begin{cases} 0 & , & M_2 = 1 , \\ \sqrt{\frac{2}{\pi}} & , & M_2 = 2 , \\ \frac{27}{8\sqrt{2\pi}} & , & M_2 = 3 , \end{cases}$$
 (21)

as given in the text.

In this limit $M_1 \gg M_2$ one can also compute the behavior of the standard deviation. Indeed from the convergence of the complex LW ensemble to the GUE (of size $M_2 \times M_2$), one has the identity in law

$$\lambda_{\text{max}} \approx \frac{1}{M_2} (M_1 - \sqrt{2M_1 \mu_{\text{max}}}) , \qquad (22)$$

where, as before, $\mu_{\rm max}$, which depends only M_2 and not on M_1 , denotes the largest eigenvalue of a GUE matrix of size $M_2 \times M_2$. This identity (22) allows to obtain straightforwardly the large M_1 behavior of the standard deviation $\Delta \lambda_{\rm max}$ as given in the text, namely

$$\Delta \lambda_{\text{max}} \approx \frac{\sqrt{2M_1}}{M_2} \Delta \mu_{\text{max}} ,$$
 (23)

where $\Delta\mu_{\text{max}}$, which depends only on M_2 , is the standard deviation of the largest eigenvalue of a GUE matrix of size $M_2 \times M_2$. It can be computed from the CDF of μ_{max} given in Eq. (20). In particular one gets

$$(\Delta\mu_{\text{max}})^2 = \begin{cases} \frac{1}{2}, & M_2 = 1, \\ 1 - \frac{2}{\pi}, & M_2 = 2, \\ \frac{3}{2} + \frac{9}{128\pi} (16\sqrt{3} - 81), & M_2 = 3. \end{cases}$$
(24)

These asymptotic behaviors in Eqs. (19)-(21) and (23)-(24) are compared to numerical and exact results in Fig. 3 of the main text, showing an excellent agreement between the different estimations.

II. WAVE PROPAGATION SIMULATIONS

In our simulations, we model wave propagation through two-dimensional (2D) diffusive slabs of size $k_0W \times k_0L$, where W and L denote the slab width and length, respectively. The sample is discretized on a 2D square grid with grid spacing $(\lambda_0/2\pi) \times (\lambda_0/2\pi)$. The dielectric constant at each grid point is defined as

$$\epsilon(\mathbf{r}) = n_0^2 + \delta \epsilon(\mathbf{r}),\tag{25}$$

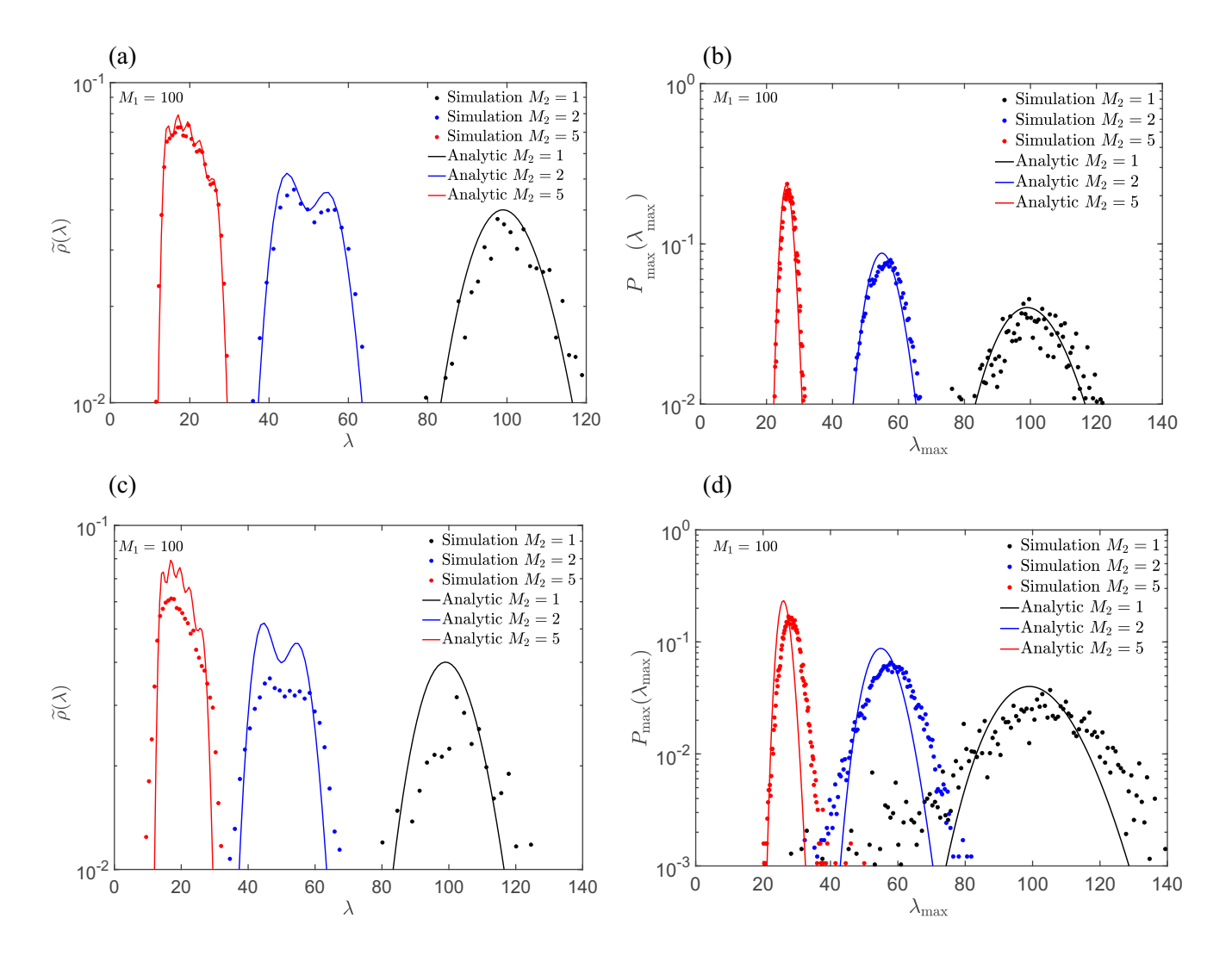


FIG. 7. (a) Eigenvalue distributions $\widetilde{\rho}(\lambda)$ and (b) largest eigenvalue distributions $P_{\max}(\lambda_{\max})$ for $M_1=100$ and $M_2=1,2,5$ for a diffusive slab with normalized thickness $k_0L=50$ and normalized transport mean free path $k_0l_t=18$. For this case, the LW–random-matrix predictions for $\widetilde{\rho}(\lambda)$ [Eq. (11)] and for $P_{\max}(\lambda_{\max})=Q'_{\max}(\lambda_{\max})$ [Eq. (18)] are in excellent agreement with the wave-propagation simulations. In contrast, for a thicker and more strongly scattering slab with $k_0L=100$ and $k_0l_t=3$, we find clear deviations between the LW–based predictions and the simulations for both $\widetilde{\rho}(\lambda)$ (c) and $P_{\max}(\lambda_{\max})$ (d).

where n_0 is the average refractive index of the medium, and $\delta\epsilon(\mathbf{r})$ is a uniformly distributed random number in the range $[-\Sigma, \Sigma]$. The slab is embedded between two homogeneous media of refractive indices n_1 and n_2 , and periodic boundary conditions are imposed along the transverse direction. The field transmission matrix t_{mn} at wavelength λ_0 is computed by solving the scalar wave equation

$$\left[\nabla^2 + k_0^2 \epsilon(\mathbf{r})\right] \psi(\mathbf{r}) = 0, \tag{26}$$

with $k_0 = 2\pi/\lambda_0$ the wavenumber corresponding to the wavelength λ_0 , using the recursive Green's function method [76, 77].

Starting from the computed transmission matrix t_{mn} , where n denotes the index of incident Fourier components

at the input and m the spatial position at the output surface of the scattering slab, we construct an ensemble of focusing operators $A^{\dagger}A$. Here, A is a randomly selected, normalized sub-transmission matrix of dimension $M_2 \times M_1$, with its variance fixed as $\text{Var}(A) = 1/M_2$. We focus on the regime $M_1 \gg M_2$, with $M_1 \in [100, 1000] \cap \mathbb{Z}$ and $M_2 \in [1, 5] \cap \mathbb{Z}$. Each sub-matrix A is formed by randomly choosing M_1 input channels and M_2 output target positions m in transmission.

For every sub-matrix size $M_2 \times M_1$, we compute the eigenvalues from

$$A^{\dagger}AV_{\alpha} = \lambda_{\alpha}V_{\alpha},\tag{27}$$

and determine the probability density $P_{\text{max}}(\lambda_{\text{max}})$, the

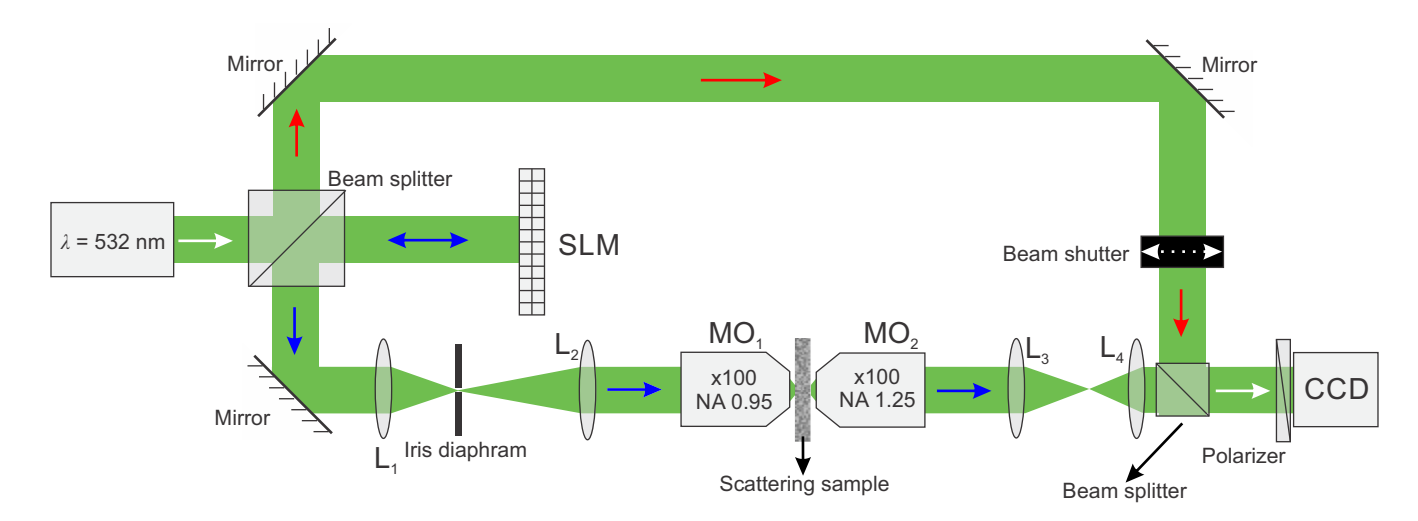


FIG. 8. Schematic of the interferometric setup. A reflective phase-only spatial light modulator (SLM) shapes the phase of a monochromatic laser beam ($\lambda_0 = 532$ nm). Using the SLM and a CCD camera, the field transmission matrix of the scattering sample is measured in k-space. $MO_{1,2}$: microscope objectives; L_{1-4} : lenses.

mean $\langle \lambda_{\text{max}} \rangle$, and the standard deviation

III. EXPERIMENTS Experimental setup and transmission-matrix

measurements $\Delta \lambda_{\rm max} = \sqrt{\langle \lambda_{\rm max}^2 \rangle - \langle \lambda_{\rm max} \rangle^2}$

(28)

of the largest eigenvalue. This procedure yields the statistical distribution of the enhancement factor for focusing light through a scattering slab. We apply it to transmission matrices t_{mn} of slabs with $k_0W = 6{,}000$, $\Sigma = 1.45, 0.65, 0.60$ (the normalized transport mean free path of $k_0 l_t = 3, 18, 20.6$, $n_0 = n_1 = n_2 = 1.5$, and normalized thicknesses $k_0L \in \{1, 50, 100, 200\}$.

Fig. 7 shows the eigenvalue distributions $\widetilde{\rho}(\lambda)$ and the largest eigenvalue distributions $P_{\text{max}}(\lambda_{\text{max}})$ obtained from LW-random-matrix theory and from wavepropagation simulations for diffusive slabs with $M_1 = 100$ and $M_2 = 1, 2, 5$. For the weakly scattering slab with $k_0L = 50$ and $k_0l_t = 18$ [panels (a,b)], the LW predictions accurately reproduce both the bulk eigenvalue density and the statistics of λ_{max} , indicating that longrange mesoscopic correlations are negligible. In contrast, for the thicker and more strongly scattering slab with $k_0L = 100$ and $k_0l_t = 3$ [panels (c,d)], clear, systematic deviations emerge in both $\widetilde{\rho}(\lambda)$ and $P_{\max}(\lambda_{\max})$. These deviations signal the breakdown of the uncorrelatedrandom-matrix assumption and reflect the growing impact of long-range mesoscopic correlations, which reshape both the eigenvalue distribution and the distribution of the largest eigenvalues.

We measure the field transmission matrix of a $\sim 10 \, \mu$ m thick layer of densely packed ZnO nanoparticles (with average diameter ~ 200 nm) deposited on a 170 µm-thick cover slip (average transmittance ~ 0.2 at $\lambda = 532$ nm) using a Mach–Zehnder interferometer (shown in Fig. 8). A linearly polarized 532-nm laser beam (Coherent, Compass 215M-50 SL) is expanded, collimated, and split into two arms; in the sample arm, the beam reflects off a spatial light modulator (Hamamatsu X10468-01) and is imaged onto the pupil of a microscope objective MO1 (Nikon 100×, NA_{in} = 0.95) by lenses L_1 ($f_1 = 100 \text{ mm}$) and L_2 ($f_2 = 250$ mm), with an iris blocking higher diffraction orders, such that each SLM segment corresponds approximately to a plane wave incident on the sample surface at a specific angle. The transmitted light is collected by an oil-immersion objective MO2 (Edmund $100 \times$, NA_{out} = 1.25), collimated by L_5 ($f_5 = 200 \text{ mm}$) and L_6 ($f_6 = 150$ mm), and interfered with the reference beam; the interference pattern is recorded at the Fourier plane of the sample output by a CCD camera (Allied Vision Manta G-031B), after a single linear polarization selection.

The transmission matrix is measured in the Hadamard basis using four-phase-shift interferometry. A circular aperture on the SLM covers 2415 segments, from which $32 \times 32 = 1024$ central segments (each 9×9 pixels) are used as input channels, while a high-frequency grating outside this region diffracts light away. Four global phase shifts, equally spaced between 0 and 2π , are applied to the Hadamard patterns to extract the relative phase with

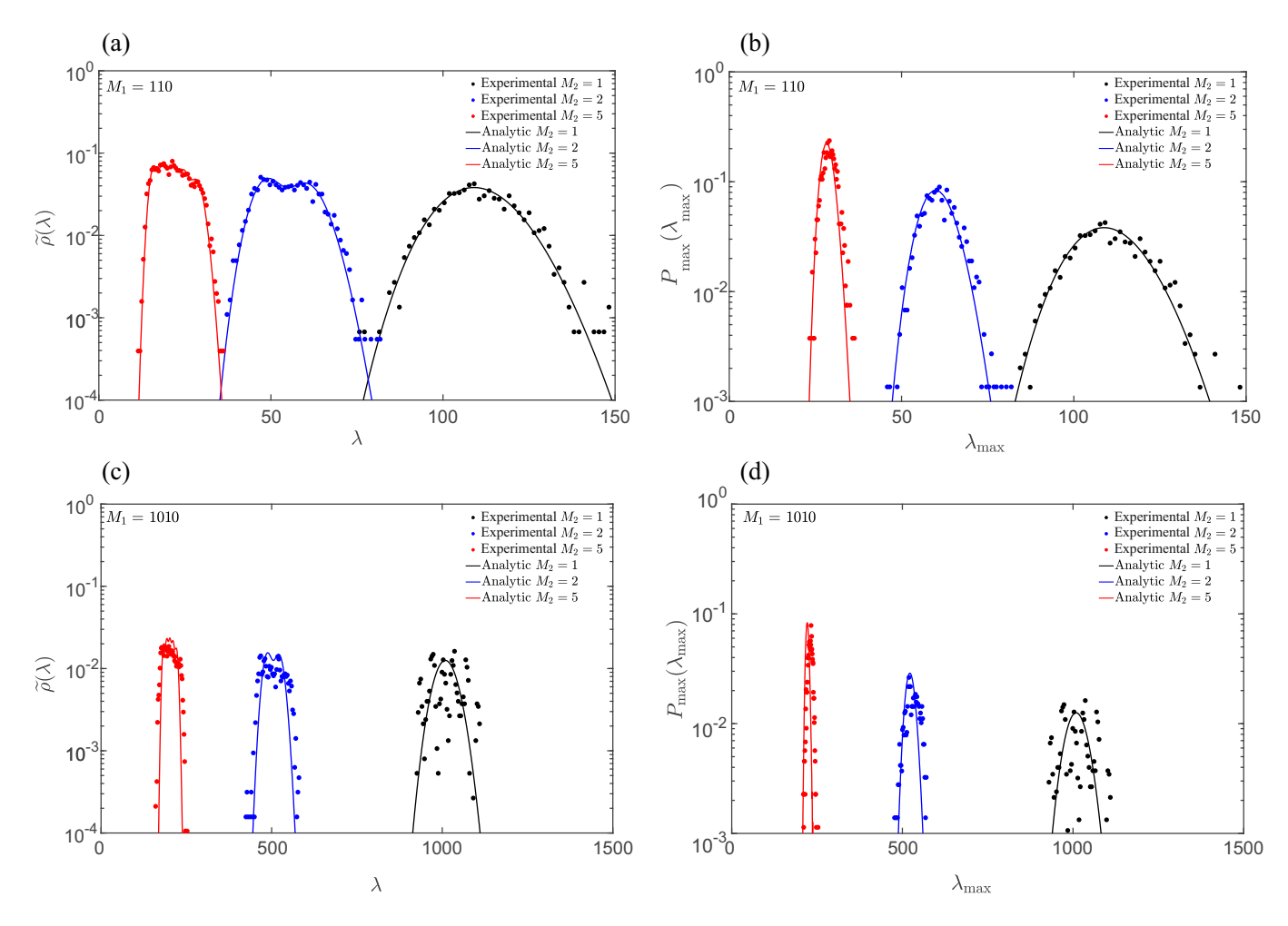


FIG. 9. (a) Eigenvalue distributions $\tilde{\rho}(\lambda)$ and (b) largest eigenvalue distributions $P_{\max}(\lambda_{\max})$ for $M_1 = 110$ and $M_2 = 1, 2, 5$ for the experimental diffusive slab. For this case, the LW–random-matrix predictions for $\tilde{\rho}(\lambda)$ [Eq. (11)] and for $P_{\max}(\lambda_{\max}) = Q'_{\max}(\lambda_{\max})$ [Eq. (18)] are in good agreement with the experimental results. In contrast, for a larger $M_1 = 1010$, we find clear deviations between the LW–based predictions and the experiments for both $\tilde{\rho}(\lambda)$ (c) and $P_{\max}(\lambda_{\max})$ (d).

the reference beam; blocking the reference allows for intensity measurements of all inputs. Combining these yields the complex transmitted field, which is detected on a $64 \times 64 = 4096$ -pixel CCD region, giving a transmission matrix $t_{m'n'}$ of size 4096×1024 . We then applied a Hadamard transform as $t_{m'n} = \sum_{n'=1}^{N} t_{m'n'} H_{n'n}$ to convert the transmission matrix into the canonical (SLM pixel) basis n. Here $H_{n'n}$ represents the unitary Hadamard transform matrix. In our experimental setup, each output index m' corresponds to a CCD camera pixel, representing a single Fourier component on the sample back surface. Since the relative phase between each output channel m' is known, a two-dimensional Fourier transform can be applied to each column of the transmission matrix $t_{m'n}$ to obtain the transmission matrix t_{mn} , where m denotes the position on the back surface of the sample, mapping the light field on the SLM to the outgoing field at the back surface of the sample.

After obtaining the experimental transmission matrix

 t_{mn} , where n denotes the SLM segment index and m the position index on the sample back surface, we construct an ensemble of randomly selected sub-transmission matrices A of size $M_2 \times M_1$. We focus on the regime $M_1 \gg M_2$, with $M_1 \in [100, 1000] \cap \mathbb{Z}$ and $M_2 \in [1, 5] \cap \mathbb{Z}$. Each sub-matrix A is formed by randomly choosing M_1 input segments on the SLM and M_2 output target positions in transmission. Since the mean transmitted intensity profile on the back surface of the sample is not spatially uniform due to diffusion, we restrict the rows of A to the central region of the diffuse spot, where the profile is approximately uniform, and select the target positions accordingly.

Experimental results

Fig. 9 presents the eigenvalue densities $\widetilde{\rho}(\lambda)$ and largest eigenvalue distributions $P_{\max}(\lambda_{\max})$ obtained from LW–random-matrix theory and from experiment.

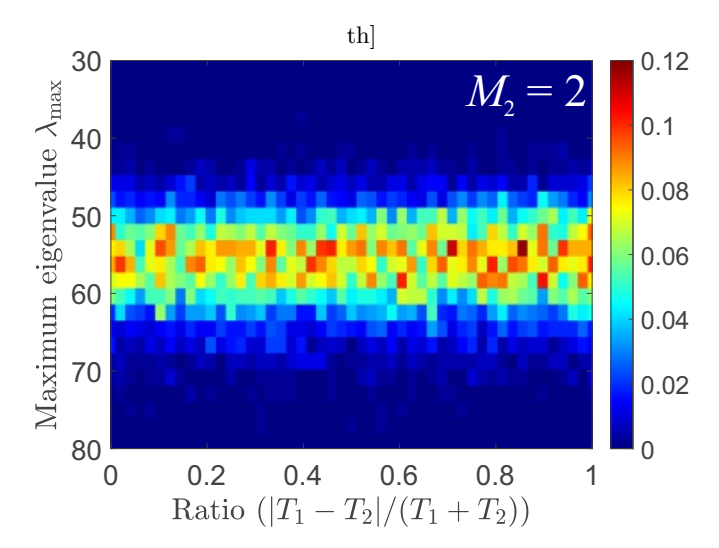


FIG. 10. Experimental joint probability density (JPD) for two-channel focusing ($M_1 = 100$, $M_2 = 2$): there is no discernible dependence between λ_{max} and the output intensity ratio, so high- λ_{max} events also occur when the two target intensities are comparable (near-equal split).

For $M_1=110$ [panels (a,b)], the LW predictions faithfully capture both the bulk eigenvalue density and the statistics of $\lambda_{\rm max}$, indicating that long-range mesoscopic correlations are negligible. In contrast, for $M_1=1010$ [panels (c,d)], pronounced and systematic deviations appear in both $\tilde{\rho}(\lambda)$ and $P_{\rm max}(\lambda_{\rm max})$. These deviations mark the breakdown of the uncorrelated random-matrix description and reveal the increasing influence of long-range mesoscopic correlations, which alter both the overall eigenvalue density and the distribution of the largest eigenvalues.

In multipoint focusing experiments, the goal is often not only to maximize the enhancement factor but also to obtain similar intensities at the target positions. It is therefore important to check whether the intensity balance between targets is correlated with the achieved enhancement. To this end, we evaluated the experimental joint probability density of the largest eigenvalue λ_{max} and the intensity imbalance for two-target focusing $(M_2=2)$, defined as $R \equiv \frac{|T_1-T_2|}{T_1+T_2}$, where T_1 and T_2 are the intensities at the two target points (Fig. 10). The analysis shows no discernible correlation between λ_{max} and R. In other words, even for large enhancement factors, one can observe either perfectly balanced intensities $(R=0,T_1=T_2)$ or completely unbalanced ones $(R=1,T_1=0)$ or $T_2=0$ with comparable likelihood.

- through opaque strongly scattering media, Opt. Lett. 32, 2309 (2007).
- [2] A. P. Mosk, A. Lagendijk, G. Lerosey, and M. Fink, Controlling waves in space and time for imaging and focusing in complex media, Nat. Photonics 6, 283– (2012).
- [3] H. Yu, J. Park, K. Lee, J. Yoon, K. Kim, S. Lee, and Y. Park, Recent advances in wavefront shaping techniques for biomedical applications, Curr. Appl. Phys. 15, 632 (2015).
- [4] I. M. Vellekoop, Feedback-based wavefront shaping, Opt. Express 23, 12189 (2015).
- [5] R. Horstmeyer, H. Ruan, and C. Yang, Guidestarassisted wavefront-shaping methods for focusing light into biological tissue, Nat. Photonics 9, 563 (2015).
- [6] S. Rotter and S. Gigan, Light fields in complex media: mesoscopic scattering meets wave control, Rev. Mod. Phys. 89, 015005 (2017).
- [7] S. Gigan, O. Katz, H. B. De Aguiar, E. R. Andresen, A. Aubry, J. Bertolotti, E. Bossy, D. Bouchet, J. Brake, S. Brasselet, et al., Roadmap on wavefront shaping and deep imaging in complex media, J. Phys. Photonics 4, 042501 (2022).
- [8] H. Cao, A. P. Mosk, and S. Rotter, Shaping the propagation of light in complex media, Nat. Phys. 18, 994 (2022).
- [9] G. Lerosey, J. De Rosny, A. Tourin, and M. Fink, Focusing beyond the diffraction limit with far-field time reversal, Science 315, 1120 (2007).
- [10] I. M. Vellekoop and A. P. Mosk, Universal optimal transmission of light through disordered materials, Phys. Rev. Lett. 101, 120601 (2008).
- [11] I. M. Vellekoop, A. Lagendijk, and A. Mosk, Exploiting disorder for perfect focusing, Nat. Photonics 4, 320 (2010).
- [12] M. Davy, Z. Shi, and A. Z. Genack, Focusing through random media: Eigenchannel participation number and intensity correlation, Phys. Rev. B 85, 035105 (2012).
- [13] M. Kim, Y. Choi, C. Yoon, W. Choi, J. Kim, Q.-H. Park, and W. Choi, Maximal energy transport through disordered media with the implementation of transmission eigenchannels, Nat. Photonics 6, 581 (2012).
- [14] M. Davy, Z. Shi, J. Wang, and A. Z. Genack, Transmission statistics and focusing in single disordered samples, Opt. Express 21, 10367 (2013).
- [15] S. M. Popoff, A. Goetschy, S. F. Liew, A. D. Stone, and H. Cao, Coherent control of total transmission of light through disordered media, Phys. Rev. Lett. 112, 133903 (2014).
- [16] O. S. Ojambati, H. Yılmaz, A. Lagendijk, A. P. Mosk, and W. L. Vos, Coupling of energy into the fundamental diffusion mode of a complex nanophotonic medium, New J. Phys. 18, 043032 (2016).
- [17] C. W. Hsu, S. F. Liew, A. Goetschy, H. Cao, and A. D. Stone, Correlation-enhanced control of wave focusing in disordered media, Nat. Phys. 13, 497 (2017).
- [18] H. Yılmaz, C. W. Hsu, A. Yamilov, and H. Cao, Transverse localization of transmission eigenchannels, Nat. Photonics 13, 352 (2019).
- [19] H. Yılmaz, C. W. Hsu, A. Goetschy, S. Bittner, S. Rotter, A. Yamilov, and H. Cao, Angular memory effect of transmission eigenchannels, Phys. Rev. Lett. 123, 203901 (2019).
- [20] I. M. Vellekoop and C. Aegerter, Scattered light fluorescence microscopy: imaging through turbid layers, Opt.

^{*} schehr@lpthe.jussieu.fr

[†] hasan.yilmaz@unam.bilkent.edu.tr

^[1] I. M. Vellekoop and A. P. Mosk, Focusing coherent light

- Lett. 35, 1245 (2010).
- [21] C. L. Hsieh, Y. Pu, R. Grange, G. Laporte, and D. Psaltis, Imaging through turbid layers by scanning the phase conjugated second harmonic radiation from a nanoparticle, Opt. Express 18, 20723— (2010).
- [22] E. G. van Putten, D. Akbulut, J. Bertolotti, W. L. Vos, A. Lagendijk, and A. P. Mosk, Scattering lens resolves sub-100 nm structures with visible light, Phys. Rev. Lett. 106, 193905 (2011).
- [23] O. Katz, E. Small, and Y. Silberberg, Looking around corners and through thin turbid layers in real time with scattered incoherent light, Nat. Photonics 6, 549—(2012).
- [24] S. A. Goorden, M. Horstmann, A. P. Mosk, B. Škorić, and P. W. Pinkse, Quantum-secure authentication of a physical unclonable key, Optica 1, 421 (2014).
- [25] S. R. Huisman, T. J. Huisman, S. A. Goorden, A. P. Mosk, and P. W. H. Pinkse, Programming balanced optical beam splitters in white paint, Opt. Express 22, 8320 (2014).
- [26] S. R. Huisman, T. J. Huisman, T. A. W. Wolterink, A. P. Mosk, and P. W. H. Pinkse, Programmable multiport optical circuits in opaque scattering materials, Opt. Express 23, 3102 (2015).
- [27] T. A. Wolterink, R. Uppu, G. Ctistis, W. L. Vos, K.-J. Boller, and P. W. Pinkse, Programmable two-photon quantum interference in 10³ channels in opaque scattering media, Phys. Rev. A 93, 053817 (2016).
- [28] T. Peng, R. Li, S. An, X. Yu, M. Zhou, C. Bai, Y. Liang, M. Lei, C. Zhang, B. Yao, and P. Zhang, Real-time optical manipulation of particles through turbid media, Opt. Express 27, 4858 (2019).
- [29] F. Wang, H. He, H. Zhuang, X. Xie, Z. Yang, Z. Cai, H. Gu, and J. Zhou, Controlled light field concentration through turbid biological membrane for phototherapy, Biomed. Opt. Express 6, 2237 (2015).
- [30] M. F. Yanik, H. Cinar, H. N. Cinar, A. D. Chisholm, Y. Jin, and A. Ben-Yakar, Functional regeneration after laser axotomy, Nature 432, 822 (2004).
- [31] L. Fenno, O. Yizhar, and K. Deisseroth, The development and application of optogenetics, Annu. Rev. Neurosci. 34, 389 (2011).
- [32] H. Ruan, J. Brake, J. E. Robinson, Y. Liu, M. Jang, C. Xiao, C. Zhou, V. Gradinaru, and C. Yang, Deep tissue optical focusing and optogenetic modulation with time-reversed ultrasonically encoded light, Sci. Adv. 3, eaao5520 (2017).
- [33] N. C. Pégard, A. R. Mardinly, I. A. Oldenburg, S. Sridharan, L. Waller, and H. Adesnik, Three-dimensional scanless holographic optogenetics with temporal focusing (3D-SHOT), Nat. Commun. 8, 1228 (2017).
- [34] S. M. Popoff, G. Lerosey, R. Carminati, M. Fink, A. C. Boccara, and S. Gigan, Measuring the transmission matrix in optics: an approach to the study and control of light propagation in disordered media, Phys. Rev. Lett. 104, 100601 (2010).
- [35] C. Prada and M. Fink, Eigenmodes of the time reversal operator: A solution to selective focusing in multipletarget media, Wave Motion 20, 151 (1994).
- [36] I. M. Vellekoop, E. G. van Putten, A. Lagendijk, and A. P. Mosk, Demixing light paths inside disordered metamaterials, Opt. Express 16, 67 (2008).
- [37] E. van Putten, A. Lagendijk, and A. Mosk, Nonimaging speckle interferometry for high-speed nanometer-scale position detection, Opt. Lett. **37**, 1070 (2012).

- [38] J. Xu, H. Ruan, Y. Liu, H. Zhou, and C. Yang, Focusing light through scattering media by transmission matrix inversion, Opt. Express 25, 27234 (2017).
- [39] Q. Feng, F. Yang, X. Xu, B. Zhang, Y. Ding, and Q. Liu, Multi-objective optimization genetic algorithm for multipoint light focusing in wavefront shaping, Opt. Express 27, 36459 (2019).
- [40] Y. Hu, M. Hu, J. Zhou, and Y. Ding, Multi-point optical focusing based on enhanced multi-objective optimized wavefront shaping, Opt. Commun. 547, 129836 (2023).
- [41] P. Hong, Y. Liang, and G. Zhang, Robust multiple focusing through scattering media via feedback wavefront shaping, Opt. Laser Technol. 176, 110939 (2024).
- [42] Z. Cheng and Y. Chen, Binary-intensity-synthetic digital optical phase conjugation for multifocal control through scattering media, Opt. Lett. 50, 5530 (2025).
- [43] S. Popoff, G. Lerosey, M. Fink, A. C. Boccara, and S. Gi-gan, Image transmission through an opaque material, Nat. Commun. 1, 81 (2010).
- [44] E. H. Zhou, H. Ruan, C. Yang, and B. Judkewitz, Focusing on moving targets through scattering samples, Optica 1, 227 (2014).
- [45] I. M. Vellekoop and A. Mosk, Phase control algorithms for focusing light through turbid media, Opt. Commun. 281, 3071 (2008).
- [46] C. W. Beenakker, Random-matrix theory of quantum transport, Rev. Mod. Phys. 69, 731 (1997).
- [47] V. A. Marčenko and L. A. Pastur, Distribution of eigenvalues for some sets of random matrices, Math. USSR Sbornik 1, 457 (1967).
- [48] M. L. Mehta, Random matrices, Vol. 142 (Elsevier, 2004).
- [49] P. J. Forrester, Log-gases and random matrices (LMS-34) (Princeton university press, 2010).
- [50] A. M. Paniagua-Diaz, W. L. Barnes, and J. Bertolotti, Wavefront shaping to improve beam quality: converting a speckle pattern into a Gaussian spot, Phys. Scr. 98, 035516 (2023).
- [51] O. S. Ojambati, J. T. Hosmer-Quint, K.-J. Gorter, A. P. Mosk, and W. L. Vos, Controlling the intensity of light in large areas at the interfaces of a scattering medium, Phys. Rev. A 94, 043834 (2016).
- [52] B. A. van Tiggelen, A. Lagendijk, and W. L. Vos, Mesoscopic theory of wavefront shaping to focus waves deep inside disordered media, Phys. Rev. A 111, 053507 (2025).
- [53] E. Akkermans and G. Montambaux, Mesoscopic Physics of Electrons and Photons (Cambridge Univ. Press, 2007).
- [54] M. J. Stephen and G. Cwilich, Intensity correlation functions and fluctuations in light scattered from a random medium, Phys. Rev. Lett. 59, 285 (1987).
- [55] S. Feng, C. Kane, P. A. Lee, and A. D. Stone, Correlations and fluctuations of coherent wave transmission through disordered media, Phys. Rev. Lett. 61, 834 (1988)
- [56] P. A. Mello, E. Akkermans, and B. Shapiro, Macroscopic approach to correlations in the electronic transmission and reflection from disordered conductors, Phys. Rev. Lett. 61, 459 (1988).
- [57] R. Pnini and B. Shapiro, Fluctuations in transmission of waves through disordered slabs, Phys. Rev. B 39, 6986 (1989).
- [58] A. Z. Genack, N. Garcia, and W. Polkosnik, Long-range intensity correlation in random media, Phys. Rev. Lett. 65, 2129 (1990).
- [59] T. Strudley, T. Zehender, C. Blejean, E. P. A. M.

- Bakkers, and O. Muskens, Mesoscopic light transport by very strong collective multiple scattering in nanowire mats, Nat. Photon. **7**, 413– (2013).
- [60] H. Yılmaz, M. Kühmayer, C. W. Hsu, S. Rotter, and H. Cao, Customizing the angular memory effect for scattering media, Phys. Rev. X 11, 031010 (2021).
- [61] Y.-K. Yu and Y.-C. Zhang, On the anti-Wishart distribution, Physica A 312, 1 (2002).
- [62] R. A. Janik and M. A. Nowak, Wishart and Anti-Wishart random matrices, J. Phys. A: Math. Gen. 36, 3629 (2003).
- [63] P. Vivo, S. N. Majumdar, and O. Bohigas, Large deviations of the maximum eigenvalue in Wishart random matrices, J. Phys. A 40, 4317 (2007).
- [64] P. Vivo, From Wishart to Jacobi ensembles: statistical properties and applications, Ph.D. thesis, Brunel University, School of Information Systems, Computing and Mathematics (2008).
- [65] S. N. Majumdar and G. Schehr, Statistics of Extremes and Records in Random Sequences (Oxford University Press, 2024).
- [66] P. A. Dighe, R. K. Mallik, and S. S. Jamuar, Analysis of transmit-receive diversity in Rayleigh fading, IEEE Trans. Commun. 51, 694 (2003).
- [67] P. J. Forrester and S. Kumar, Recursion scheme for the largest β-Wishart-Laguerre eigenvalue and Landauer conductance in quantum transport, J. Phys. A: Math. Theor. 52, 42LT02 (2019).
- [68] C. A. Tracy and H. Widom, Level-spacing distributions and the Airy kernel, Commun. Math. Phys. 159, 151 (1994).
- [69] K. Johansson, Shape fluctuations and random matrices, Commun. Math. Phys. 209, 437 (2000).
- [70] I. M. Johnstone, On the distribution of the largest eigenvalue in principal components analysis, Ann. Stat. 29, 295 (2001).
- [71] S. N. Majumdar and G. Schehr, Top eigenvalue of a ran-

- dom matrix: large deviations and third order phase transition, J. Stat. Mech.: Theory Exp. **2014** (1), P01012.
- [72] K. A. Takeuchi, M. Sano, T. Sasamoto, and H. Spohn, Growing interfaces uncover universal fluctuations behind scale invariance, Sci. Rep. 1, 34 (2011).
- [73] M. Fridman, R. Pugatch, M. Nixon, A. A. Friesem, and N. Davidson, Measuring maximal eigenvalue distribution of Wishart random matrices with coupled lasers, Phys. Rev. E 85, 020101 (2012).
- [74] G. Makey, S. Galioglu, R. Ghaffari, E. D. Engin, G. Yıldırım, Ö. Yavuz, O. Bektaş, Ü. S. Nizam, Ö. Akbulut, Ö. Şahin, et al., Universality of dissipative selfassembly from quantum dots to human cells, Nat. Phys. 16, 795 (2020).
- [75] R. Sarma, A. Yamilov, P. Neupane, B. Shapiro, and H. Cao, Probing long-range intensity correlations inside disordered photonic nanostructures, Phys. Rev. B 90, 014203 (2014).
- [76] A. MacKinnon, The calculation of transport properties and density of states of disordered solids, Z. Phys. B 59, 385 (1985).
- [77] H. U. Baranger, D. P. DiVincenzo, R. A. Jalabert, and A. D. Stone, Classical and quantum ballistic-transport anomalies in microjunctions, Phys. Rev. B 44, 637 (1991).
- [78] A. Goetschy and A. D. Stone, Filtering random matrices: the effect of incomplete channel control in multiple scattering, Phys. Rev. Lett. 111, 063901 (2013).
- [79] H. Yu, T. R. Hillman, W. Choi, J. O. Lee, M. S. Feld, R. R. Dasari, and Y. Park, Measuring large optical transmission matrices of disordered media, Phys. Rev. Lett. 111, 153902 (2013).
- [80] D. Gaspard and A. Goetschy, Radiant field theory: A transport approach to shaped wave transmission through disordered media, Phys. Rev. Lett. 135, 033804 (2025).
- [81] D. Gaspard and A. Goetschy, Transmission eigenvalue distribution in disordered media from radiant field theory, Phys. Rev. Research 7, 033071 (2025).